Force analysis of a soft-rigid hybrid pneumatic actuator and its application in a bipedal inchworm robot

Zhujin Jiang and Ketao Zhang

Centre for Advanced Robotics, School of Engineering and Materials Science, Queen Mary University of London, London E1 4NS, UK
Corresponding author: Ketao Zhang; E-mail: ketao.zhang@qmul.ac.uk

Abstract

This paper systematically investigates a soft-rigid hybrid pneumatic actuator (SRHPA), which consists of a rigid-foldable twisting skeleton capable of a large range of helical motion and a soft bellows muscle with high linear driving force. Considering the unique varying-pitch helical motion of the foldable skeleton, the analytical model mapping the input force generated by the bellows muscle and output forces of the actuator is revealed and verified with a simulation of the force analysis. Prototypes of the actuator are developed by fabricating the twisting skeleton with multilayered aluminum composite panels and 3D-printing the bellows muscle with thermoplastic polyurethane (TPU) 95A filament. The static and dynamic performances of the prototypes are tested to validate the analytical modeling of output forces. Using the actuator as a module, a novel bipedal inchworm robot with four modules is developed and tested to demonstrate its adaptability in confined space by switching between the going-straight, the turning-around, and the rotating gaits. The hybrid actuator and the inchworm robot with zero onboard electronics have the potential to be deployed in extreme environments where pneumatically actuated systems are preferred over electrical machines and drives, such as in nuclear and explosive environments.

1. Introduction

Soft fluidic actuators were categorized as a subset of soft actuators and exhibit excellent characteristics such as inherent compliance, good impact resistance, high energy-to-weight ratio, and safety interaction with humans [1, 2]. Based on the mode of motion, they can be further classified mainly into linear actuators [3, 4], bending actuators [5–7], and torsional actuators [8–10]. In particular, twisting actuators capable of the compound motion of rotation and contraction have also been developed and combined to achieve other motions, including linear, rotational, and radial movements [11, 12]. For instance, inspired by the compliant Wren mechanism, twisting actuators were developed by integrating elastic materials in a soft chamber for medical applications [13], but their maximum angular displacement is only 40° (13° demonstrated in the experiments) and the maximum operating pressure is only 90 kPa. In contrast, the twisting actuators composed of two compliant Wren mechanisms in ref. [14] were developed by additive manufacturing and can only achieve a limited range of rotation (9°). Their output forces have not been investigated. Besides, inspired by the Kresling origami, the twisting actuators in ref. [15] are driven by vacuum and have a bistable property with a rotation of 73°, meaning that they can hardly be controlled precisely to the transitory positions between two stable states. Along with this design approach, Jiao et al. fabricated vacuum-powered twisting actuators with silicone rubbers with a maximum twisting angle of 80°. These twisting actuators were used as modules to assemble mobile robots, such as the pipe-climbing robot and the modular quadruped robot [16]. Compared to the twisting actuators in refs. [11, 16] which have one fully compressed state and can rotate from the fully compressed state to the fully deployed state in a single direction, the twisting actuators developed in ref. [17] are bidirectional

---

and can switch between tristable states (one fully deployed state and two fully folded states) based on the actuating sequences, but their deformation is accompanied by bending motion. In summary, the aforementioned twisting actuators are actuated by low positive pneumatic pressure or vacuum, thereby generating low output forces. They are soft and flexible, resulting in difficulties in analytical modeling and unwanted forms of deformation [18]. To increase the stiffness and ensure the desired motions of soft actuators, soft-rigid hybrid actuators which incorporate rigid skeletons with physical constraints into soft actuators [19, 20] attract much attention. For instance, soft-rigid hybrid linear actuators [21, 22], bending actuators [23], and rotary actuators [24, 25] were developed for a variety of applications. Further, the conceptual design of a soft-rigid hybrid pneumatic actuator (SRHPA) was proposed using the modified Wren parallel mechanism with four identical UU (U: universal joint) limbs [26, 27] as the twisting skeleton, and its helical motion was revealed based on screw theory [28–31] in our early work [32].

Soft fluidic actuators have been used to develop soft robots, which have increased potential for resilience to perturbations, safe human–robot interaction, and adaptability to various hostile environments [33, 34]. For instance, the untethered soft robot [35] fabricated with silicone rubbers can adapt to harsh environmental conditions such as snowstorms, fires, and water and is capable of a speed of 0.0077 body length per second (*BL/s*). The quadruped soft robot [36] fabricated by soft lithography can navigate difficult obstacles using crawling and undulation gaits with manual control. However, the body structure made from soft materials is highly flexible and continuous, bringing additional challenges in precise kinematic modeling and motion control [33]. By contrast, inspired by the musculoskeletal systems in nature [37, 38], pneumatically actuated soft-rigid hybrid-legged robots [39, 40] exhibited promising capabilities in building precise kinematics models like rigid-bodied robots and adapting to various environments like soft-legged robots. For example, the soft-rigid hybrid quadruped robot in refs. [41, 42] adapted to speed variation by adjusting its stride and cyclic duration, but the robot needs human assistance during walking. Further, with the rigid exoskeleton providing structural support and the soft pneumatic joints providing actuation and inherent compliance to external forces, soft-rigid hybrid-legged robots, including bipedal robots [43, 44], quadruped robots [45, 47], and hexapod robots [48], with simple gaits were proposed. There are still challenges in designing soft-rigid hybrid robots driven by pneumatic artificial muscles and developing appropriate controllers for agile movements.

In this paper, to reduce the unwanted deformation, improve the rotational range and output forces, and address the challenges in modeling soft twisting actuators, we systematically develop and investigate a SRHPA based on the design concept presented in our early work [32] and utilize the actuator for developing a novel bipedal inchworm robot.

In the following sections, the characteristics of the helical motion of the SRHPA are first analyzed. Section 3 reveals the analytical model of the output forces of the SRHPA. Simulation is implemented to validate this theoretical analysis. In Section 4, the static and dynamic performances of the proposed actuator are evaluated with experimental tests, and its analytical model mapping the input force and output forces is further verified. Section 5 demonstrates the development of the SRHPA-integrated inchworm robot with three different gaits and related control strategies. Its adaptability in navigating through confined spaces is also presented. Section 6 provides a detailed discussion of this work, and Section 7 concludes the paper.

2. The SRHPA with helical motion

By integrating a rigid-foldable twisting skeleton with a soft bellows muscle, the proposed SRHPA shown in Fig. 1(a) is able to achieve helical motion [32]. The twisting skeleton determines the helical motion of the actuator. The bellows muscle connecting the base and platform of the twisting skeleton generates linear force to drive the twisting skeleton, thus producing output forces.

Figure 1(b) illustrates the twisting skeleton's kinematic structure. The base and the platform of the twisting skeleton are identical squares □ABCD with center O and □EFGH with center O', respectively. The twisting skeleton has four identical limbs and is symmetrical with respect to OO' which is
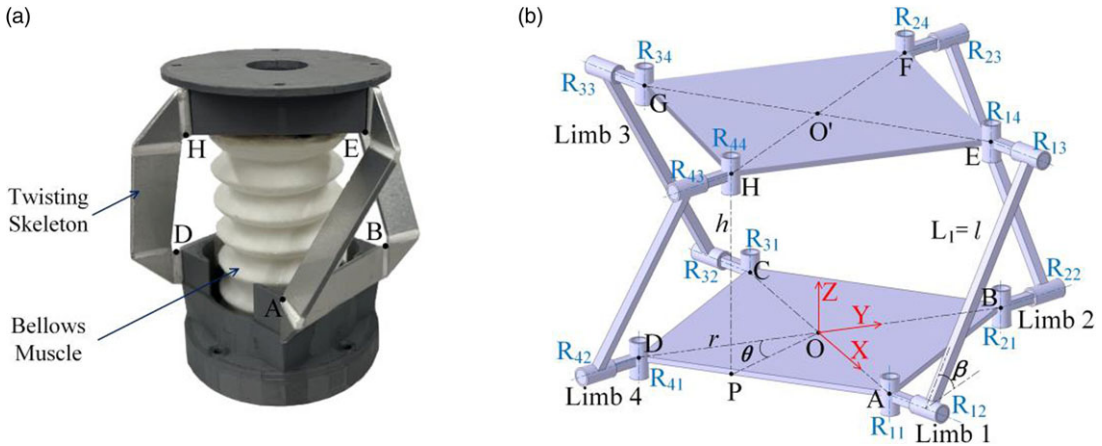
Figure 1. *(a) Prototype of the SRHPA with design parameters $l = \sqrt{2}r = 45$ mm. (b) Kinematic structure of the twisting skeleton.*

perpendicular to the platform. In each limb, the axes of revolute joints R_{i1} and R_{i4} ($i = 1,2,3,$ and 4) are perpendicular to the base, while the axes of the revolute joints R_{i2} and R_{i3} are parallel to each other as well as the base.

A Cartesian coordinate frame $O - XYZ$ is set up at the base where the origin of the reference frame is coincident with the center O. The X-axis and Y-axis pass points A and B, respectively, and the Z-axis follows the right-hand rule. The angular displacement of the moving platform corresponding to the base is denoted by θ. It can be measured between lines OD and OP where P is the projection of vertex H on the base. The distance between the platform □EFGH and the base □ABCD is denoted by h. The length of the link L_1 connecting the revolute joints R_{12} and R_{13} is defined as l. The angle between the link L_1 and the base is denoted by β. The radius of the excircle of the base □ABCD is denoted by r.

Based on the motion-screw system [32] of the moving platform, the actuator is able to achieve helical motion along OO' with a pitch of h_p:

$$h_p = r \cdot \cot \beta \cdot \cos \frac{\theta}{2} \tag{1}$$

where

$$\beta = \arccos \left(\frac{2r}{l} \cdot \sin \frac{\theta}{2} \right) \tag{2}$$

Besides, the rotational range of the actuator is determined by the design parameters l and r. According to the geometric design of the skeleton, the distance d between the lines AE and BF of the two adjacent Limbs 1 and 2 is given by:

$$d = |\boldsymbol{r}_{ab} \cdot \boldsymbol{n}| / |\boldsymbol{n}| \tag{3}$$

where

$$\boldsymbol{r}_{ab} = (-r, r, 0)^{\mathrm{T}} \tag{4}$$

$$\boldsymbol{n} = \left(1 + s\theta - c\theta, 1 - s\theta - c\theta, \frac{2r}{h}(1 - c\theta) \right)^{\mathrm{T}} \tag{5}$$

$\boldsymbol{r}_{ab}$ is the vector of the line AB. $\boldsymbol{n}$ is the common perpendicular of the vectors of the lines AE and BF. 's' and 'c' are the abbreviations of sin(∗) and cos(∗), respectively.

Assuming that actuators rotate from the initial position where the exoskeleton is fully extended and $\theta = 0°$, the correlation between the distance d and the angular displacement θ of the actuators with different design parameters in Fig. 2(a) reveals that the actuators reach the maximum angular displacement
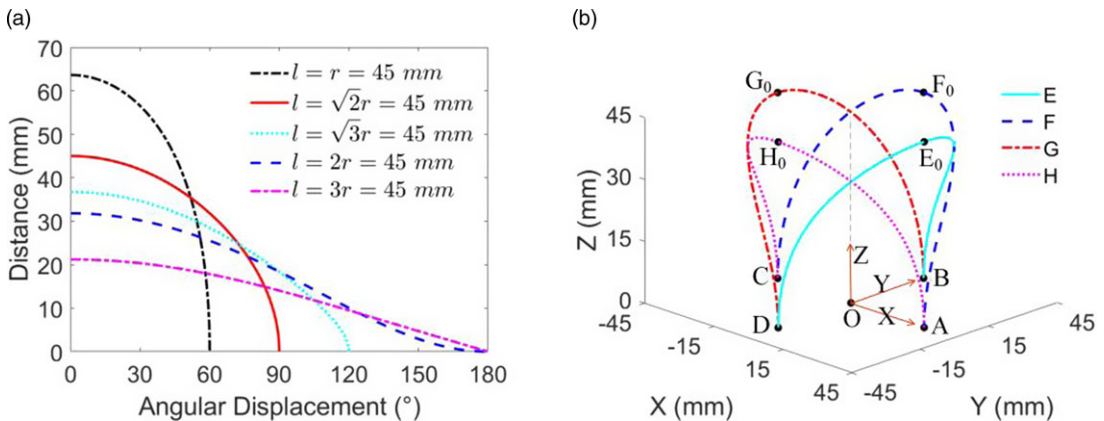
Figure 2. *(a) The correlation between actuators' distance d and the angular displacement θ with different design parameters. (b) 3D trajectories of the vertices E, F, G, and F of the actuator with design parameters $l = \sqrt{2}r = 45\,mm$.*

when the distance $d = 0$, where the two limbs collide. When increasing the ratio l / r, the maximum angular displacement of the actuators increases and finally reaches 180° ($l / r \geq 2$).

In order to achieve a large rotational range and ensure enough space between the moving platform and the base for integrating an artificial muscle, a balanced trade-off is to set $l = \sqrt{2}r$. As a result, the largest angular displacement in a single rotating direction is 90° without physical interference between any two adjacent limbs.

While Fig. 2(a) illustrates the angular displacement of the actuators rotating from the initial position in a single direction, the actuator is able to rotate clockwise and anticlockwise from the initial position. The 3D trajectories of vertices E, F, G, and H of the actuator with design parameters $l = \sqrt{2}r = 45$ mm are drawn in Fig. 2(b) where E_0, F_0, G_0, and H_0 denote the transitory positions of vertices E, F, G, and H at the angular displacement of 0°, respectively. For instance, if the actuator rotates anticlockwise, the vertex E moves from E_0 to B along the solid curve (cyan color). If it rotates clockwise, the vertex E moves from E_0 to D. Hence, the actuator with design parameters $l = \sqrt{2}r$ can achieve a rotation of 90° from the fully deployed state to one of the fully folded states. It can rotate 180° in principle from one fully folded state to another fully folded state in a single direction.

3. Force analysis and simulation of the SRHPA

3.1. Analytical model of the output forces

To formulate the output forces as a function of the input force from the bellows muscle of the SRHPA, the following assumptions are made: all links of the actuator are regarded as rigid bodies; the moving platform is lightweight and its weight and inertial are ignored in the modeling.

Based on the constraint-screw system of the moving platform derived in our early work [32], we can further derive that the i-th limb ($i = 1,2,3$, and 4) applies two geometric constants to the moving platform of the actuator. One of the geometric constraints is a constraint force aligned to AE, BF, CG, or DH. Another is a constraint torque which is parallel to the base and perpendicular to the axis of the joint R_{i2} ($i = 1,2,3$, and 4).

The free-body diagrams of Limb 1 and the platform are shown in Figs. 3(a) and (b), respectively. The driving force generated by the bellows muscle is denoted by F_a. The force and torque constraints that the i-th limb exerts on the platform are denoted by F_i and M_i, respectively. Assuming that an external force load F_z acting along OO' and an external torque load M_z around OO' are applied on the platform, it derives
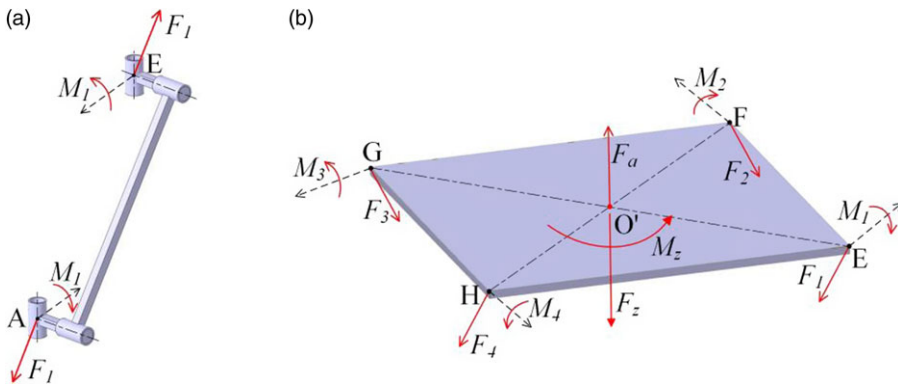
Figure 3. *Free-body diagrams for force analysis of the actuator subject to the driving force F_a, external force F_z, and external torque M_z. (a) Constraints applied to limb 1. (b) Constraints applied to the moving platform.*

$$\sum_{i=1}^{4} F_i \cdot \sin \beta = F_a - F_z \tag{6}$$

$$\sum_{i=1}^{4} F_i \cdot \cos \beta \cdot \cos \frac{\theta}{2} \cdot r = M_z \tag{7}$$

$$\sum_{i=1}^{4} M_i = 0 \tag{8}$$

Substituting Eq. (6) into Eq. (7), it yields

$$\frac{M_z}{F_a - F_z} = r \cdot \cot \beta \cdot \cos \frac{\theta}{2} \tag{9}$$

Equation (9) reveals the output force and the output torque of the actuator, which are equal to the force load F_z and the torque load M_z, respectively, are related to the driving force F_a. It implies that the proportionality coefficient between the torque M_z and the resultant force $F_a - F_z$ (PCTF) depends on the angular displacement θ and the design parameters r and l of the actuator. The PCTF indicates the capability of the actuator to convert the driving force into output torque. Comparing Eqs. (1) and (9), it further concludes that the PCTF equals the pitch of the actuator.

3.2. Simulation of the output forces

The software ADAMS® is used to verify the force analysis of the actuator. Firstly, two 3D models of the twisting skeleton of the actuator with design parameters $l = \sqrt{2}r = 30$ mm and $l = \sqrt{2}r = 45$ mm are designed in 3D software CATIA® and then imported into ADAMS®. The revolute joint is employed on all hinges R_{ij} ($i = 1,2,3$, and 4, $j = 1,2,3$, and 4), and a fixed joint is added to the base, as illustrated in Fig. 4(a). To validate the analytical model given in Eq. (9), a constant force F_z of 100 N and a constant torque M_z of 1 Nm are applied to the platform of the actuator along OO'. As motions must be set on joints in ADAMS®, a cylindrical joint is applied to the platform with respect to the base, and a translational motion with a speed of 4 mm/s is defined for the cylindrical joint to represent the actuation of the bellows muscle.

After setting constraints, simulations are conducted (Supplementary Video S1). The driving force F_a on the left side of Eq. (9) and the angular displacement θ are measured simultaneously during simulation. The PCTF is calculated automatically by the software. Figure 4(b) shows that the PCTF increases with the increase of the angular displacement, and the analytical model of actuators given in Eqn. (9) coincides with the simulation data (red dots and stars).
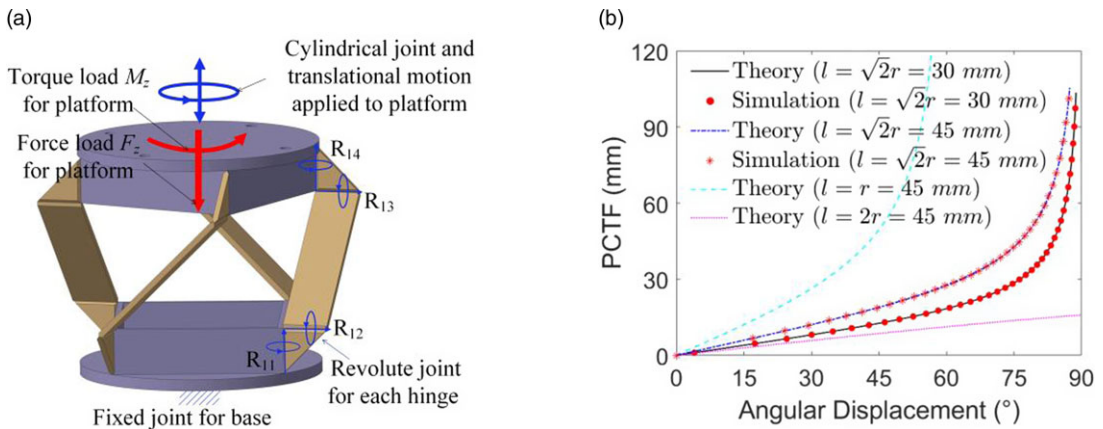
Figure 4. *(a) Constraint settings of the actuator for simulation. (b) Simulation of the PCTF of actuators at different angular displacements.*
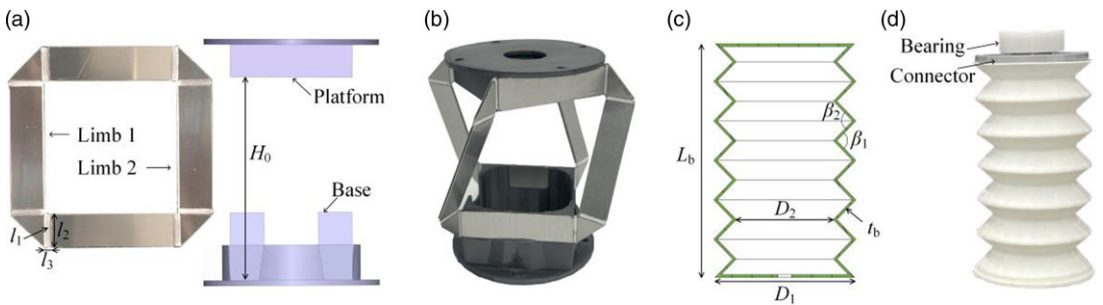

Figure 5. *Fabrication process of the SRHPA. (a) A sample of two limbs bonded with the platform and the base. (b) A sample of the twisting skeleton. (c) Dimension of the bellows muscle in section view. (d) A prototype of the bellows muscle bonded with a rolling bearing and a bearing connector.*

4. Experimental evaluations of static and dynamic performances of the SRHPA

4.1. Prototyping of the SRHPA

The limbs of the twisting skeleton are CNC machined using the aluminum composite panel (HYLITE) with a polypropylene core and aluminum cover layers by removing specified aluminum cover layers, as shown in Fig. 5(a). The limbs are then adhered to the platform and the base to obtain the twisting skeleton (Fig. 5(b)). Besides, the bellows muscle (Fig. 5(c)) is 3D-printed based on fused deposition modeling. Thermoplastic polyurethane (TPU) 95A filament is selected as the printing material due to its wear and tear resistance and rubber-like flexibility. The printing settings can refer to our previous work [49]. The actuator is completed by fixing the end of the bellows muscle with an air inlet to the base of the twisting skeleton and connecting the other end of the bellows muscle to the platform of the twisting skeleton with a rolling bearing and a bearing connector, as shown in Fig. 5(d). The bellows muscle can be inflated and vacuumed, thereby pushing or pulling the twisting skeleton to generate output forces. The design parameters of the actuator for prototyping are listed in Table I.

4.2. Experimental setup

To measure the output force generated by the actuator, a connector with a rolling bearing inside is designed to connect the platform of the actuator with the gripper of the Instron machine 5967, while the

Table I. *Design parameters of the SRHTA for prototyping*

Twisting skeleton			Bellows muscle		
Sym.	Physical quantity	Value	Sym.	Physical quantity	Value
r	Radius of the connection points	31.8 mm	L_b	Design length	69 mm
l	Length of the limbs	45 mm	n	Number of chambers	6
H_0	Length of space for the muscle	69 mm	D_1	Outer diameter	40 mm
l_1	Thickness of the hinges	1.6 mm	D_2	Inner diameter	28 mm
l_2	Length of the hinges	12 mm	t_b	Thickness	0.9 mm
l_3	Width of the hinges	1.6 mm	β_1	Exterior angle	97.98°
			β_2	Interior angle	97.98°

base of the actuator is fixed to the load cell of the Instron machine via two clamps, as shown in Fig. 6(a). The Instron machine controls the length h of the actuator.

To measure the pure torque generated by the actuator and verify the analytical model derived in Eq. (9), a customized testing platform shown in Fig. 6(b) is built. A 6-axis torque-force sensor (ROBOTOUS RFT40-SA01) is used to connect the base of the actuator to the left plate of the testing platform, while the platform of the actuator is connected with a spool. With two linear ball bearings inside, the spool is able to translate and rotate along the central shaft. A string connected to the spool is used to load calibration weights. The actuator contracts when it is loaded without pressurized air input. On the contrary, the actuator extends when it is inflated without loading. The actuator achieves a balance if the driving force generated by the bellows muscle equals the external load. Besides, a laser distance sensor, Banner Q4XTBLAF300Q8, installed at the right plate of the testing platform, is used to measure the displacement of the spool, which can be transformed into the angular displacement θ of the actuator.

To measure the actuating response of the actuator, three markers are attached to the top of the actuator, as shown in Fig. 6(c). Its movement is measured by the motion capture system OptiTrack.

4.3. Tests of the static force and torque
The output force of the actuator is tested by inflating/vacuuming the actuator with a constant pressure and moving the gripper of the Instron machine down to control the length of the actuator (Fig. 6(a)). The output force of the actuator is recorded. Figure 6(d) shows that for a given positive pressure, the output force gradually increases with the increase of the angular displacement. This results from the inherent stiffness of the actuator and the increased contact area between the bellows muscle and the twisting skeleton. The actuator can generate a force of 200 N under a pressure of 150 kPa. Besides, the output force of the actuator under negative pressures is denoted by negative values. Figure 6(d) illustrates that for a given negative pressure, the absolute value of the output force decreases with the increase of the angular displacement due to the decreased vacuum space inside the bellows muscle.

Using the testing platform shown in Fig. 6(b), the output torque of the actuator at different angular displacements is tested by inflating or vacuuming the actuator with a constant pressure and loading different calibration weights to the spool, as illustrated in Fig. 6(e). (As the actuator shown in Fig. 1 rotates clockwise during inflation, the output torque of the actuator along the direction of **O'O** is denoted by positive values). Figure 6(e) shows that for a given positive pressure, increasing the angular displacement leads to increased output torque. The actuator can generate a torque of 2.2 Nm with the angular displacement changing from 44° to 90° by adjusting the pressure from 150 to –45 kPa. Besides, the actuator under a pressure of –45 kPa produces a torque of –0.75 Nm at the angular displacement of 69°. Table II shows that the proposed actuator has the largest rotational range, output force, and torque compared with existing pneumatic twisting actuators capable of the compound motion of rotation and contraction. Note that the proposed actuator needs to pass the fully deployed state to complete a full rotation of 180°, which is not the focus of this work and will be explored in our future work.

Table II. *Comparison of the SRHPA with existing pneumatic twisting actuators capable of the compound motion of rotation and contraction.*

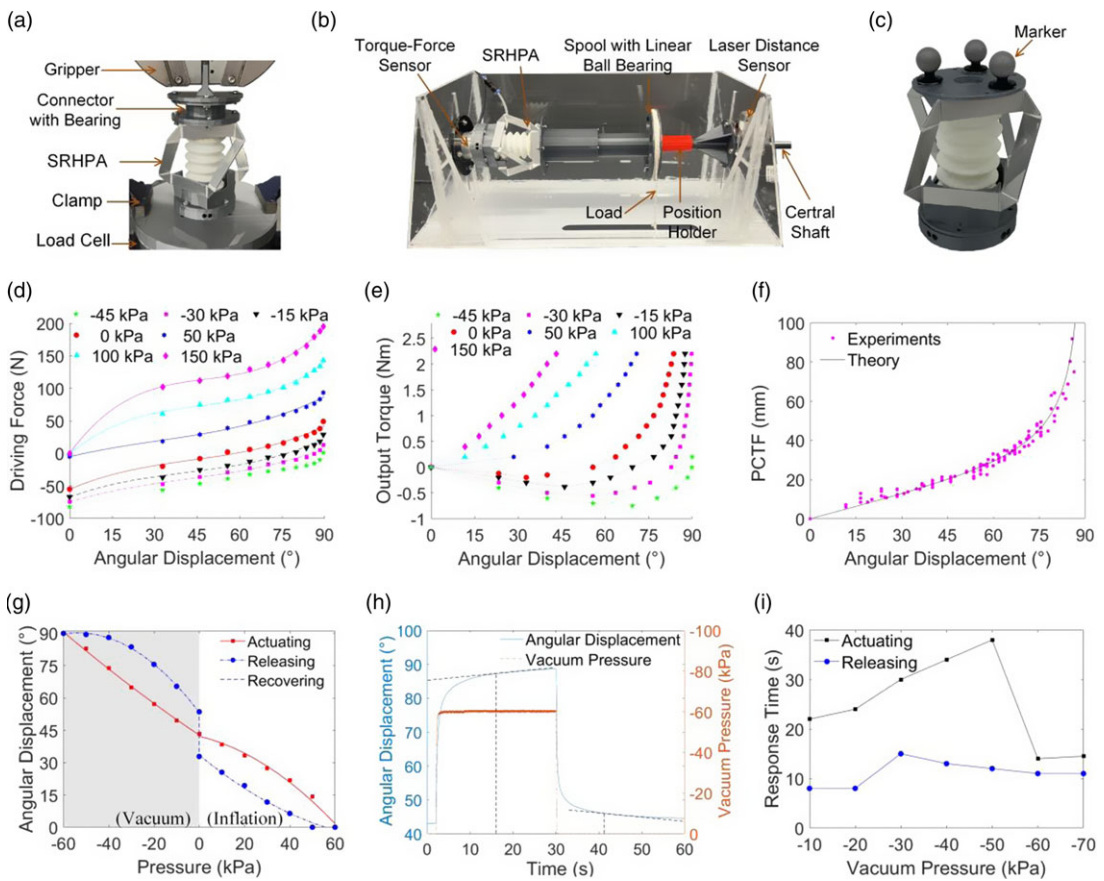| Actuators	Actuation	Rotation (°)	Force (N)	Torque (Nm)	Length (mm)
Proposed SRHPA	Inflation/vacuum	180	200	2.2	85
Soft actuator [15]	Vacuum	73	20	N/A	30
Twisting actuator [11]	Vacuum	120	47	0.225	60
Artificial muscle [16]	Vacuum	80	N/A	N/A	40
Pneumatic actuator [14]	Inflation	9	N/A	N/A	42.6
Rotary actuator [13]	Inflation	14	N/A	N/A	40

Figure 6. *Experimental validation of the SRHPA. (a) Force test of the actuator via Instron 5967. (b) Torque test and analytical model verification of the actuator. (c) Evaluation of the actuating response of the actuator. (d) Output force of the actuator at different angular displacements. (e) Output torque of the actuator at different angular displacements. (f) PCTF of the actuator at different angular displacements. (g) Angular displacement of the actuator at different air pressures. (h) Actuating response of the angular displacement of the actuator at a pressure of –60 kPa. (i) Actuating/releasing response time of the actuator under different vacuum pressures.*

4.4. Verification of the input and output forces

The testing platform shown in Fig. 6(b) is used to verify the analytical model of the actuator given in Eq. (9). First, the actuator is inflated with a constant pressure, and the spool is loaded by a calibration

weight to compress the actuator. When the actuator is in static equilibrium, the force load F_z and torque load M_z applied on the actuator are measured by the torque-force sensor. (The force load results from the friction between the central shaft and the spool.) The position of the actuator is recorded by the laser distance sensor, and the position holder is installed between the spool and the right plate of the testing platform to maintain the actuator at the same position. Next, the calibration weight is removed, and the driving force of the actuator, F_a, is measured by the torque-force sensor. The PCTF of the actuator at the corresponding angular displacement is calculated. Then the calibration weight and the pressure supplied to the actuator are changed, and the above steps are repeated.

The PCTF of the actuator at different angular displacements shown in Fig. 6(f) reveals that the experimental data (magenta dots) match well with the theoretical model (dark solid plot). The mean absolute error (MAE) of the PCTF between the experimental data and the theoretical model is 2.8 mm. Thus, the theoretical model of output forces of the actuator in Eq. (9) is proved.

4.5. Evaluation of the actuating response

With three markers attached to the top of the actuator (Fig. 6(c)), the angular displacement of the actuator at different pressures during actuating and releasing processes is measured. Figure 6(g) shows that in the actuating process, the angular displacement increases from 43.1° to 90° with the change of the pressure from 0 to –60 kPa and decreases from 43.1° to 0° with the increase of the pressure from 0 to 60 kPa. In the releasing process, adjusting the pressure from –60 kPa to 0 leads to the decrease of the angular displacement from 90° to 53.5°, and decreasing the pressure from 60 kPa to 0 results in the increased angular displacement from 0° to 32.8°. An evident hysteresis between the actuating and releasing processes can be observed. The difference between the starting point of the actuating process and the ending point of the releasing process is due to the compliance of the hinges of the twisting skeleton and the bellows muscle. The state from the ending point of the releasing process to the starting point of the actuating process is defined as the recovering process, marked in the dashed plot in Fig. 6(g). During this recovering process, if an external force is applied to set the actuator back to its original position and then released, the actuator stays at its original position permanently.

The response characteristics of the actuator under vacuum pressure are essential for its potential applications where rotational movement is required. Figure 6(h) demonstrates that when the actuator is vacuumed with a pressure of –60 kPa, the angular displacement changes sharply at the beginning and varies slowly at the end. The duration from the beginning of inflation/deflation to the change rate of the angular displacement reaching 0.1/-0.1 is defined as actuating/releasing response time. For example, it can be seen from Fig. 6(h) that under a pressure of –60 kPa, the actuating response time of the actuator is 14 s (starts at 2 s with the beginning of inflation and ends at 16 s with the change rate of the angular displacement of 0.1), and the releasing response time is 11 s (starts at 30 s with the beginning of deflation and ends at 41 s with the change rate of the angular displacement of –0.1). The correlation between the actuating/releasing response time and the vacuum pressure in Fig. 6(i) illustrates that the actuating response time gradually increases with the change of the pressure from –10 to –50 kPa, but it rapidly drops to 14 s at the pressure of –60 kPa. By contrast, the releasing response time of the actuator under different vacuum pressures fluctuates.

5. Application of the SRHPA in a novel bipedal inchworm robot

5.1. Design of the bipedal inchworm robot

To demonstrate the potential applications of the SRHPA, a bipedal inchworm robot with a dimension of $320 \times 190 \times 90$ mm at a fully deployed configuration is designed by combining four actuators, two connectors and two anchors, as shown in Fig. 7(a). The actuators and anchors of the inchworm robot are marked as A1–A6, respectively. When vacuumed, A3 rotates in the opposite direction of the other three actuators, that is, A2, A4, and A5. Thus, the robotic body composed of A3 and A4 achieves pure contraction without any relative rotation when A3 and A4 are vacuumed at the same condition. The anchors A1 and A6 consist of a soft suction cup and a rigid cover. The rigid cover is used to support the
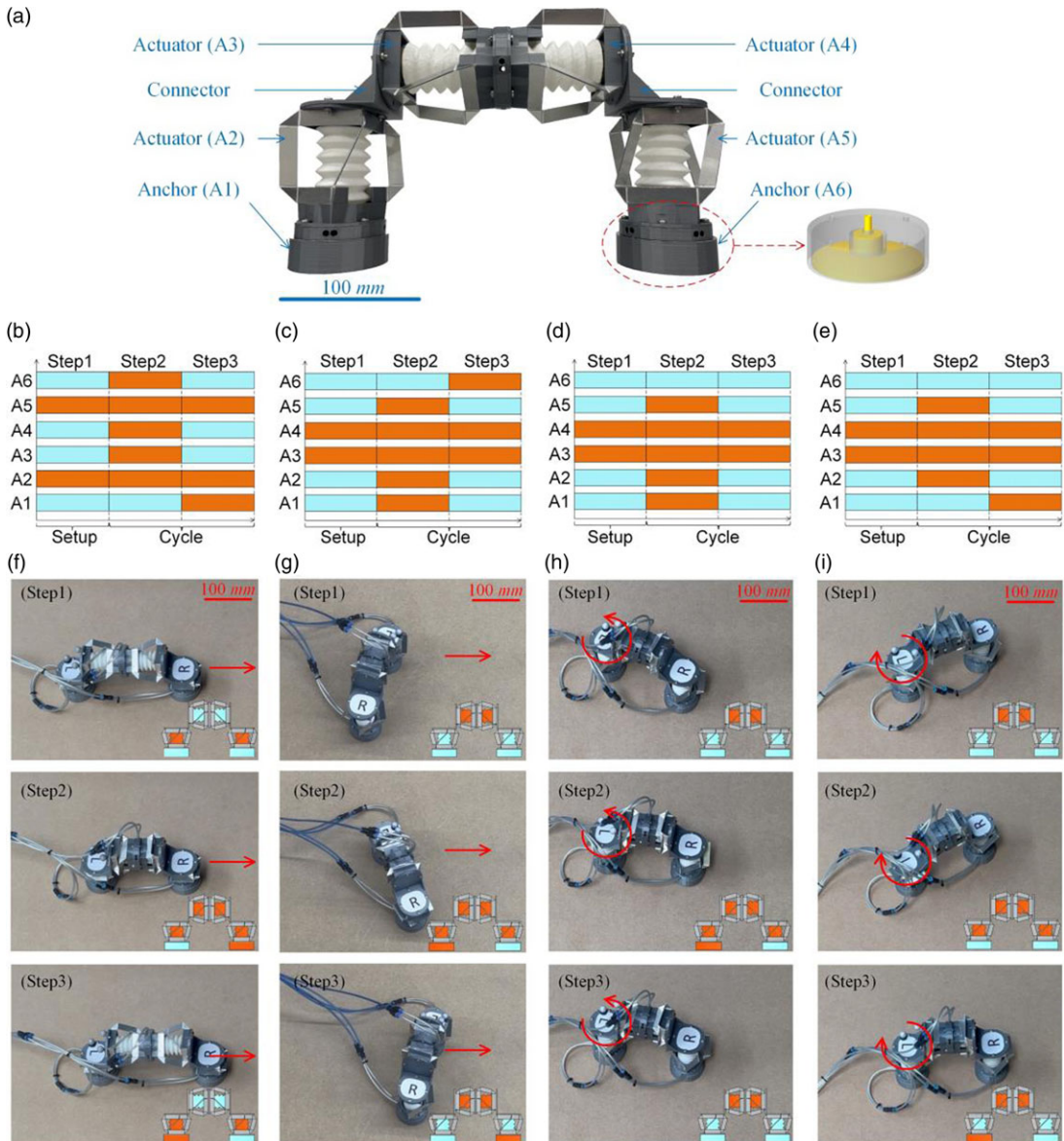
Figure 7. *The SRHPA-integrated bipedal inchworm robot. (a) Prototype of the bipedal inchworm robot. (b) Actuating sequence of the inchworm robot with the going-straight gait. (c) Actuating sequence of the inchworm robot with the turning-around gait. (d) Actuating sequence of the inchworm robot with anti-clockwise rotation around the axis of A1. (e) Actuating sequence of the inchworm robot with clockwise rotation around the axis of A1. (f) The working process of the inchworm robot with the going-straight gait. (g) The working process of the inchworm robot with the turning-around gait. (h) The working process of the inchworm robot with anticlockwise rotation around the axis of A1. (i) The working process of the inchworm robot with clockwise rotation around the axis of A1.*

inchworm robot, and the soft suction cup enables the adhesion between the anchor and the ground when vacuumed. The actuators are fixed to connectors with screws to assemble the robot. Solenoid valves (VDW350-5G-4-02F-Q) controlled by Arduino Uno Rev3 are used to adjust the actuating and releasing states of the actuators and suckers where vacuum pressure is applied at the actuating state. There is no

pressure supplied at the releasing state. Three markers are attached to the left leg of the inchworm robot to record its position and rotation via the motion capture system OptiTrack.

5.2. Going-straight gait of the inchworm robot

The inchworm robot is able to achieve linear movement via the going-straight gait (Supplementary Video S1). Figure 7(b) and (f) illustrate the actuation sequence of A1–A6 for the going-straight gait, where the orange portions represent the actuating state and the blue portions denote the releasing state. (Vacuum pressure is applied at the actuating state, while no pressure is supplied at the releasing state.) In Step 1, A2 and A5 are actuated first to lower the center of mass of the inchworm robot, thus increasing stability. Then, A3, A4, and A6 are actuated, leading to the robotic body of the inchworm robot contracting and dragging A1 (Step 2). Next, A1 is actuated while A3, A4, and A6 are released (Step 3). The anchor A6 moves forward during the recovery of A3 and A4. By repeating Steps 2 and 3, the inchworm robot can move forward continuously. Further, the inchworm robot moves backward by actuating A1, A3, and A4 first and then actuating A6.

The vacuum pressure, actuating time, and releasing time affect the movement speed of the inchworm robot, and their influences are shown in Fig. 8(a)-(c), respectively. It can be seen from Fig. 8(a) that the movement speed increases with higher vacuum pressure. Increasing the actuating time leads to a longer stride at each cycle, as shown in Fig. 8(b). Figure 8(c) illustrates that a maximum speed of 16 mm/s is achieved using the going-straight gait under the conditions of -70 kPa vacuum pressure, 2.5 s actuating time, and 0.5 s releasing time, which is equivalent to 0.05 BL/s.

5.3. Turning-around gait of the inchworm robot

The bipedal inchworm robot is capable of achieving linear movement via the turning-around gait (Supplementary Video S1). The actuation sequence of the inchworm robot with the turning-around gait is shown in Fig. 7(c) and (g). During Step 1, A3 and A4 can be actuated first to reduce the resisting moment of the inchworm robot for later movement. Then, A1, A2, and A5 are actuated, resulting in the inchworm robot rotating anticlockwise along the axis of A1 (Step 2). Next, A6 is actuated while A1, A2, and A5 are released, leading to the inchworm robot rotating in the reverse direction along the axis of A6 (Step 3). By repeating Steps 2 and 3, the inchworm robot is able to move forward continuously.

The results show that the vacuum pressure (Fig. 8(d)), actuating (Fig. 8(e)), and releasing time affect the movement speed of the inchworm robot when implementing the turning-around gait. The maximum speed of 17.5 mm/s under the conditions of -70 kPa vacuum pressure, 2.5 s actuating time, and 1 s releasing time can be seen in Fig. 8(d), equivalent to 0.076 BL/s. (The body length is 230 mm when both A3 and A4 are vacuumed.) Figure 8(e) shows that the stride of the inchworm robot at each cycle varies by changing the actuating time.

5.4. Rotating gait of the inchworm robot

The bipedal inchworm robot can realize rotational movement via the rotating gait (Supplementary Video S1). The actuation sequence of the inchworm robot with anticlockwise rotation along the axis of A1 is shown in Fig. 7(d) and (h). The actuation sequence of the inchworm robot with clockwise rotation along the axis of A1 is similar and illustrated in Fig. 7(e) and 7(i).

The vacuum pressure, actuating time, and releasing time affect the rotational speed of the inchworm robot. Figure 8(f) shows that the maximum rotational speed of the inchworm robot anticlockwise rotating around the axis of A1 is 6.7 °/s under the conditions of -70 kPa vacuum pressure, 2.5 s actuating time, and 1 s releasing time, while Fig. 8(h) indicates that the maximum rotational speed of the inchworm robot clockwise rotating around the axis of A1 is 8 °/s under the conditions of -70 kPa vacuum pressure, 1.5 s actuating time, and 1 s releasing time. Further, the rotational angle per cycle during anticlockwise and clockwise rotation mainly depends on the actuating time, as shown in Fig. 8(g) and (i), respectively.
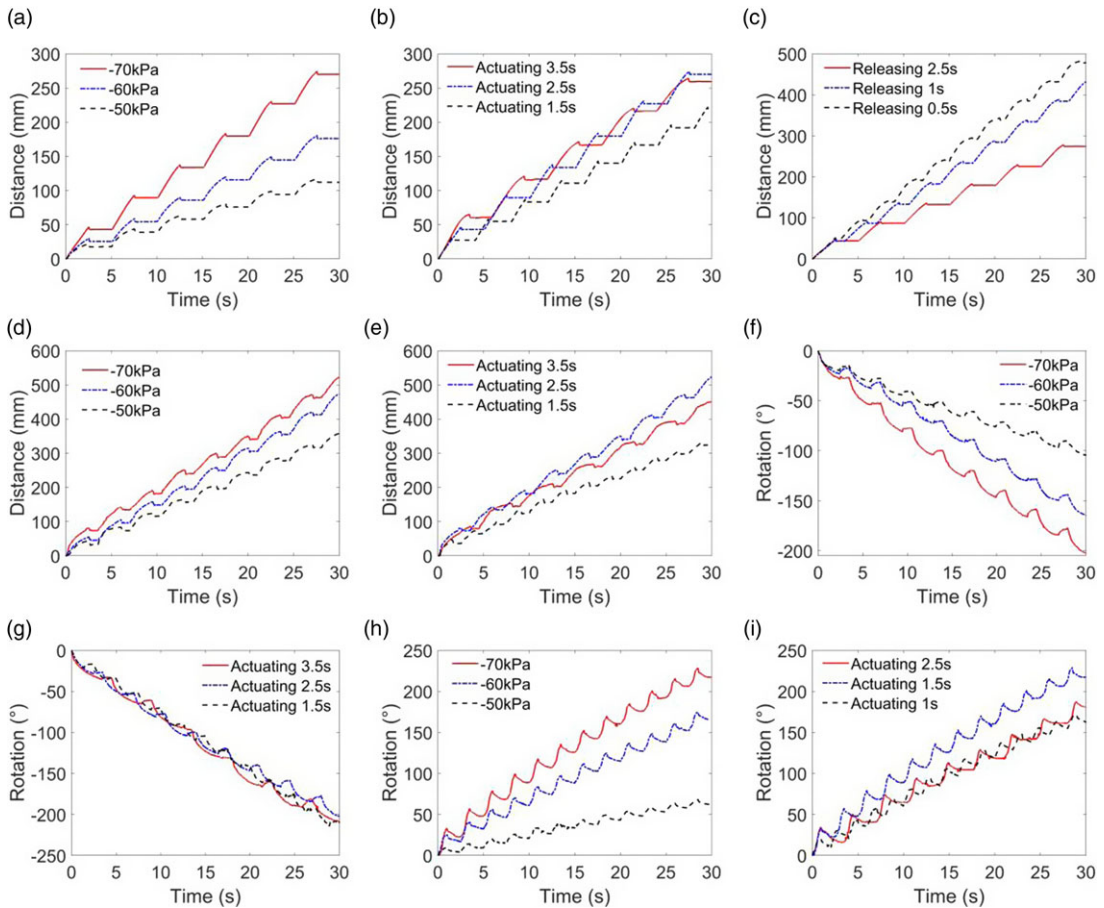
Figure 8. *Movement and rotation of the inchworm robot. (a) Going-straight gait under different vacuum pressures given 2.5 s actuating time and 2.5 s releasing time. (b) Going-straight gait at different actuating times given –70 kPa vacuum pressure and 2.5 s releasing time. (c) Going-straight gait at different releasing times given –70 kPa vacuum pressure and 2.5 s actuating time. (d) Turning-around gait under different vacuum pressures given 2.5 s actuating time and 1 s releasing time. (e) Turning-around gait at different actuating times given –70 kPa vacuum pressure and 1 s releasing time. (f) Anticlockwise rotation under different vacuum pressures given 2.5 s actuating time and 1 s releasing time. (g) Anticlockwise rotation at different actuating times given –70 kPa vacuum pressure and 1 s releasing time. (h) Clockwise rotation under different vacuum pressures given 1.5 s actuating time and 1 s releasing time. (i) Clockwise rotation at different actuating times given –70 kPa vacuum pressure and 1 s releasing time.*

The inchworm robot is capable of rotating around the axis of A6 anticlockwise and clockwise. More details can be referred to Supplementary Video S1. Further, compared to existing pneumatically actuated mobile robots listed in Table III, the proposed inchworm robot is competitive in maximum locomotion speed and maximum rotational speed, and it is easily assembled and controlled with an open-loop controller to navigate via different gaits.

5.5. Navigation in confined space

To demonstrate the advantages of the inchworm robot by switching different gaits, its locomotion in confined space is implemented, as shown in Fig. 9 (Supplementary Video S1). Firstly, the robot moves forward using the turning-around gait. When arriving at the corner, it changes to the rotating gait to

Table III. *Comparison of the inchworm robot with existing pneumatically-actuated mobile robots.*

| Robots	Movement (BL/s)	Rotation (°/s)	Use of the actuator	Advantages	Limitations
Proposed robot	0.076	8	SRHPA	High speed, simple control, flexibility on flat terrains.	Difficult to move on rough terrains.
Untethered robot [35]	0.0077	0.2	Pneumatic network	Adaptability to adverse environments including snow, water, and fire.	Slow locomotion speed, difficulty in modeling.
Multigait robot [36]	0.053	N/A	Pneumatic network	Simple design and control to generate mobility.	Difficulties in predictive modeling and motion control.
Quadruped robot [50]	0.069	N/A	Bending actuator	Capability to climb bending rods.	Cannot produce enough force to overcome the friction caused by rods.
Hexapod robot [51]	0.05	N/A	Viscous fluid-driven actuator	The feet can be placed anywhere within its 2D workspace.	Movement in one direction, difficulty in modeling.
Omnidirectional Robot [52]	0.033	1.63	Soft cylinder	Capable of translational motion and rotation.	Low accuracy of motion.
Hyper-redundant robot [53]	0.08	3.5	Foam-based actuator	Reconfigurability, multimodal locomotion.	Nominal use at standard atmospheric pressure.
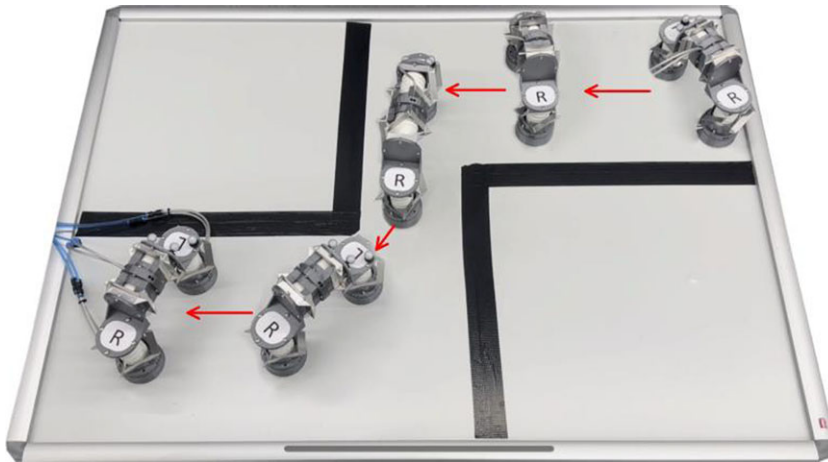
Figure 9. *Navigation of the inchworm robot in the confined space.*

adjust its orientation. Once parallel to the aisle, the inchworm robot switches to the going-straight gait to move forward since the length of the inchworm robot is shorter than the width of the aisle. It can be seen from Fig. 9 that the trajectory of the inchworm robot using the going-straight gait is not straight since the inchworm robot is lightweight and its movement is influenced by the tubes. After passing the aisle, the inchworm robot walks via the turning-around gait as the space is wide enough.

6. Discussions

The twisting skeleton of the actuator has a singular position at the fully deployed state with an angular displacement of $0°$, and it can be rotated clockwise and anticlockwise manually at this singular position to achieve a complete rotation of $180°$. It needs additional actuators to work along with the bellows muscle to drive the twisting skeleton crossing the singular position. Once the actuator stays at the singular position in static equilibrium, it can hardly be compressed by only vacuuming the bellows muscle. Hence, when inflating the bellows muscle to push the twisting skeleton, the pressurized air should be adequately controlled to prevent the actuator from reaching its singular position.

The inherent stiffness of the actuator, mainly resulting from the bellows muscle and the hinges of the twisting skeleton, affects the locomotion speed of the inchworm robot. To reduce the inherent stiffness of the actuator and improve the locomotion speed of the inchworm robot, flexible materials such as Ecoflex, textiles, and TPU membranes can be considered for fabricating the bellows muscle, and the thickness of the 3D-printed bellows muscle can be decreased. However, these approaches will downgrade the output forces of the actuator since the bellows muscle fabricated with low modulus materials with a reduced thickness cannot withstand high pressure and may have air leaking issues.

Further, 3D printing technology is used to fabricate the bellows muscle. The material selection, the shape and thickness of the bellows muscle, the accuracy of the 3D printer, and printing settings affect the bellows muscle's performances, including its stiffness, airtightness, compression ratio, maximum operating pressure, etc. In particular, more robust 3D printing technology is required to facilitate high-quality bellows muscles as the current printing technologies have a low success rate in making bellows muscles airtight under high pressure.

7. Conclusions

This paper presented the theoretical modeling, simulation verification, experimental evaluation, and an example application of the soft-rigid hybrid pneumatic actuator (SRHPA) which integrates a

rigid-foldable twisting skeleton capable of helical motion with a soft bellows muscle capable of large linear force. The force analysis of the actuator revealed its capability of converting force generated by the linear bellows muscle into torque around the axis of linear displacement. Both simulation and experiments validated this theoretical analysis, enabling a simplified analytical model of the actuator for motion control and scalability of size and output forces.

With CNC-machined twisting skeleton using aluminum composite panels and 3D-printed bellows muscle using TPU 95A filament, the actuator with design parameters $l = \sqrt{2}r = 45$ mm can generate a maximum force of 200 N and a maximum torque of 2.2 Nm, respectively. It demonstrated precise motion, a 90° rotational range in a single rotational direction, and high output forces compared to existing pneumatic twisting actuators, as given in Table II.

A novel bipedal inchworm robot was designed by integrating four SRHPAs and two suckers. The robot is able to achieve linear movement via the going-straight gait at a maximum speed of 0.05 BL/s and via the turning-around gait at a maximum speed of 0.076 BL/s, and realize rotational movement utilizing the rotating gait with a maximum rotational speed of 8 °/s. The test results showed that the robot's performance is competitive with existing pneumatically actuated mobile robots (Table III). The proposed SRHPA and SRHPA-integrated inchworm robot have the potential to be deployed in environments where pneumatically actuated systems are preferred over electrical machines and drives, such as in nuclear, explosive, and magnetic resonance environments.

Future work will focus on designing actuation systems to drive the proposed actuator to cross its singular position, thereby achieving a complete rotation of 180° from one fully folded state to another fully folded state in a single direction. Novel robots based on the actuator will also be developed to achieve complex functions and movements.

References

[1] A. Pagoli, F. Chapelle, J.-A. Corrales-Ramon, Y. Mezouar and Y. Lapusta, "Review of soft fluidic actuators: Classification and materials modeling analysis," *Smart Mater. Struct.* **31**(1), 013001 (2021).

[2] P. Polygerinos, N. Correll, S. A. Morin, B. Mosadegh, C. D. Onal, K. Petersen, M. Cianchetti, M. T. Tolley and R. F. Shepherd, "Soft robotics: Review of fluid-driven intrinsically soft devices; manufacturing, sensing, control, and applications in human-robot interaction," *Adv. Eng. Mater.* **19**(12), 1700016 (2017).

[3] G. Belforte, G. Eula, A. Ivanov and A. L. Visan, "Bellows textile muscle," *J. Text. Inst.* **105**(3), 356–364 (2014).

[4] H. D. Yang, B. T. Greczek and A. T. Asbeck, "Modeling and analysis of a high-displacement pneumatic artificial muscle with integrated sensing," *Front. Robot. AI* **5**, 136 (2019).

[5] L. Guo, K. Li, G. Cheng, Z. Zhang, C. Xu and J. Ding, "Design and experiments of pneumatic soft actuators," *Robotica* **39**(10), 1806–1815 (2021).

[6] G. Bao, L. Chen, Y. Zhang, S. Cai, F. Xu, Q. Yang and L. Zhang, "Trunk-like soft actuator: Design, modeling, and experiments," *Robotica* **38**(4), 732–746 (2020).

[7] J. Hu, L. Liang and B. Zeng, "Design, modeling, and testing of a soft actuator with variable stiffness using granular jamming," *Robotica* **40**(7), 2468–2484 (2022).

[8] S. Aziz and G. M. Spinks, "Torsional artificial muscles," *Mater. Horiz.* **7**(3), 667–693 (2020).

[9] S. Sanan, P. S. Lynn and S. T. Griffith, "Pneumatic torsional actuators for inflatable robots," *J. Mech. Robot.* **6**(3), 031003 (2014).

[10] W. Xiao, D. Hu, W. Chen, G. Yang and X. Han, "A new type of soft pneumatic torsional actuator with helical chambers for flexible machines," *J. Mech. Robot.* **13**(1), 011003 (2021).

[11] Z. Jiao, C. Ji, J. Zou, H. Yang and M. Pan, "Vacuum-powered soft pneumatic twisting actuators to empower new capabilities for soft robots," *Adv. Mater. Technol.* **4**(1), 1800429 (2019).

[12] D. Li, D. Fan, R. Zhu, Q. Lei, Y. Liao, X. Yang, Y. Pan, Z. Wang, Y. Wu and S. Liu, "Origami-inspired soft twisting actuator," *Soft Robot.* **10**(2), 395–409 (2023).

[13] T. Gayral, L. Rubbert and P. Renaud, "Modeling and Identification for the Design of a Rotary Soft Actuator Based on Wren Mechanism". **In:** *2019 IEEE/RSJ International Conference on Intelligent Robots and Systems (IROS)* (2019) pp. 7453–7459.

[14] L. Rubbert, F. Schuler, T. Gayral, M. de Wild and P. Renaud, "Development of models for additively manufactured actuators using compliant Wren mechanism," *Precis. Eng.* **72**, 304–314 (2021).

[15] T. Jin, L. Li, T. Wang, G. Wang, J. Cai, Y. Tian and Q. Zhang, "Origami-inspired soft actuators for stimulus perception and crawling robot applications," *IEEE Trans. Robot.* **38**(2), 748–764 (2021).

[16] Z. Jiao, C. Zhang, W. Wang, M. Pan, H. Yang and J. Zou, "Advanced artificial muscle for flexible material-based reconfigurable soft robots," *Adv. Sci.* **6**(21), 1901371 (2019).

[17] Z. Jiao, C. Zhang, J. Ruan, W. Tang, Y. Lin, P. Zhu, J. Wang, W. Wang, H. Yang and J. Zou, "Re-foldable origami-inspired bidirectional twisting of artificial muscles reproduces biological motion," *Cell Rep. Phys. Sci.* **2**(5), 100407 (2021).

[18] J. Yan, X. Zhang, B. Xu and J. Zhao, "A new spiral-type inflatable pure torsional soft actuator," *Soft Robot.* **5**(5), 527–540 (2018).

[19] S. Li, D. M. Vogt, D. Rus and R. J. Wood, "Fluid-driven origami-inspired artificial muscles," *Proc. Natl. Acad. Sci.* **114**(50), 13132–13137 (2017).

[20] T. Ranzani, S. Russo, F. Schwab, C. J. Walsh and R. J. Wood. "Deployable Stabilization Mechanisms for Endoscopic Procedures" **In:** *2017 IEEE International Conference on Robotics and Automation (ICRA)* (2017) pp. 1125–1131.

[21] M. J. Mendoza, S. D. Gollob, D. Lavado, B. H. B. Koo, S. Cruz, E. T. Roche and E. A. Vela, "A vacuum-powered artificial muscle designed for infant rehabilitation," *Micromachines* **12**(8), 971 (2021).

[22] J.-G. Lee and H. Rodrigue, "Origami-based vacuum pneumatic artificial muscles with large contraction ratios," *Soft Robot.* **6**(1), 109–117 (2019).

[23] J. Zhang, T. Wang, J. Wang, M. Y. Wang, B. Li, J. X. Zhang and J. Hong, "Geometric confined pneumatic soft-rigid hybrid actuators," *Soft Robot.* **7**(5), 574–582 (2020).

[24] J. Yi, X. Chen, C. Song, J. Zhou, Y. Liu, S. Liu and Z. Wang, "Customizable three-dimensional-printed origami soft robotic joint with effective behavior shaping for safe interactions," *IEEE Trans. Robot.* **35**(1), 114–123 (2018).

[25] L. Paterno, G. Tortora and A. Menciassi, "Hybrid soft-rigid actuators for minimally invasive surgery," *Soft Robot.* **5**(6), 783–799 (2018).

[26] G. Kiper and E. Söylemez, "Modified Wren platforms," In 13th IFToMM world congress, Guanojuato, Mexico (2011).

[27] J. Wang, X. Kong and J. Yu, "Design of deployable mechanisms based on Wren parallel mechanism units," *J. Mech. Des.* **144**(6), 063302 (2022).

[28] E. R. Leal and J. S. Dai. "From Origami to a New Class of Centralized 3-DOF Parallel Mechanisms." **In:** *International Design Engineering Technical Conferences and Computers and Information in Engineering Conference* (2007) pp. 1183–1193.

[29] J. S. Dai, Z. Huang and H. Lipkin, "Mobility of overconstrained parallel mechanisms," *J. Mech. Des.* **128**(1), 220–229 (2006).

[30] J. A. Saglia, N. G. Tsagarakis, J. S. Dai and D. G. Caldwell, "A high-performance redundantly actuated parallel mechanism for ankle rehabilitation," *Int. J. Robot. Res.* **28**(9), 1216–1227 (2009).

[31] J.-S. Zhao, H.-L. Sun, X. Sun, Z.-H. Ma and S.-B. Zhang, "Screw statics of spatial structures and mechanisms," *Structures* **55**, 411–426 (2023).

[32] Z. Jiang and K. Zhang. "A novel torsional actuator augmenting twisting skeleton and artificial muscle for robots in extreme environments." **In:** *2021 IEEE International Conference on Robotics and Automation (ICRA)* (2021) pp. 9318–9324.

[33] D. Rus and M. T. Tolley, "Design, fabrication and control of soft robots," *Nature* **521**(7553), 467–475 (2015).

[34] Z. Liu, Y. Wang, J. Wang and Y. Fei, "Design and locomotion analysis of modular soft robot," *Robotica* **40**(11), 3995–4010 (2022).

[35] T. TolleyMichael, F. ShepherdRobert, C. GallowayKevin, J. WoodRobert and M. WhitesidesGeorge, "A resilient, untethered soft robot," *Soft Robot.* **1**(3), 213–223 (2014).

[36] R. F. Shepherd, F. Ilievski, W. Choi, S. A. Morin, A. A. Stokes, A. D. Mazzeo, X. Chen, M. Wang and G. M. Whitesides, "Multigait soft robot," *Proc. Natl. Acad. Sci.* **108**(51), 20400–20403 (2011).

[37] X. Dong, Y. Wang, X.-J. Liu and H. Zhao, "Development of modular multi-degree-of-freedom hybrid joints and robotic flexible legs via fluidic elastomer actuators," *Smart Mater. Struct.* **31**(3), 035034 (2022).

[38] R. Sato, E. Kazama, A. Ming, M. Shimojo, F. Meng, H. Liu, X. Fan, X. Chen, Z. Yu and Q. Huang. "Design and Control of Robot Legs with Bi-articular Muscle-Tendon Complex," **In:** *2017 IEEE International Conference on Robotics and Biomimetics (ROBIO)* (2017) pp. 2605–2610.

[39] A. Nemiroski, Y. Y. Shevchenko, A. A. Stokes, B. Unal, A. Ainla, S. Albert, G. Compton, E. MacDonald, Y. Schwab and C. Zellhofer, "Arthrobots," *Soft Robot.* **4**(3), 183–190 (2017).

[40] J. Fan, S. Wang, Y. Wang, G. Li, J. Zhao and G. Liu, "Research on frog-inspired swimming robot driven by pneumatic muscles," *Robotica* **40**(5), 1527–1537 (2022).

[41] Y. Fukuoka, Y. Habu, K. Inoue, S. Ogura and Y. Mori, "Autonomous speed adaptation by a muscle-driven hind leg robot modeled on a cat without intervention from brain," *Int. J. Adv. Robot. Syst.* **18**(5), 17298814211044936 (2021).

[42] Y. Fukuoka, R. Komatsu, K. Machii, M. Yokota, M. Tobe, A. N. Ibrahim, T. Fukui and Y. Habu, "Pace running of a quadruped robot driven by pneumatic muscle actuators: An experimental study," *Appl. Sci.* **12**(9), 4146 (2022).

[43] B. Verrelst, R. V. Ham, B. Vanderborght, F. Daerden, D. Lefeber and J. Vermeulen, "The pneumatic biped "Lucy" actuated with pleated pneumatic artificial muscles," *Auton. Robot.* **18**(2), 201–213 (2005).

[44] B. Vanderborght, B. Verrelst, R. Van Ham and D. Lefeber, "Controlling a bipedal walking robot actuated by pleated pneumatic artificial muscles," *Robotica* **24**(4), 401–410 (2006).

[45] B. Gorissen, E. Milana, A. Baeyens, E. Broeders, J. Christiaens, K. Collin, D. Reynaerts and M. De Volder, "Hardware sequencing of inflatable nonlinear actuators for autonomous soft robots," *Adv. Mater.* **31**(3), 1804598 (2019).

[46] Y. Yamada, S. Nishikawa, K. Shida, R. Niiyama and Y. Kuniyoshi, "Neural-Body Coupling for Emergent Locomotion: A Musculoskeletal Quadruped Robot with Spinobulbar Model," **In:** *2011 IEEE/RSJ International Conference on Intelligent Robots and Systems*(2011) pp. 1499–1506.

[47] A. Hunt, N. Szczecinski and R. Quinn, "Development and training of a neural controller for hind leg walking in a dog robot," *Front. Neurorobot.* **11**, 18 (2017).

[48] S. T. Mahon, A. Buchoux, M. E. Sayed, L. Teng and A. A. Stokes, "Soft Robots for Extreme Environments: Removing Electronic Control." **In:** *2nd IEEE International Conference on Soft Robotics (RoboSoft)*(2019) pp. 782–787.

[49] Z. Jiang, C. Liu and K. Zhang. "A Variable Stiffness Continuum Parallel Manipulator With 3D Printed Pneumatic Artificial Muscles," **In:** *International Design Engineering Technical Conferences and Computers and Information in Engineering Conference*(2022) p. V007T07A057.

[50] N. Zhu, H. Zang, B. Liao, H. Qi, Z. Yang, M. Chen, X. Lang and Y. Wang, "A quadruped soft robot for climbing parallel rods," *Robotica* **39**(4), 686–698 (2021).

[51] Y. Matia, G. H. Kaiser, R. F. Shepherd, A. D. Gat, N. Lazarus and K. H. Petersen, "Harnessing nonuniform pressure distributions in soft robotic actuators," *Adv. Intell. Syst.* **5**(2), 2200330 (2023).

[52] J. Zou, Y. Lin, C. Ji and H. Yang, "A reconfigurable omnidirectional soft robot based on caterpillar locomotion," *Soft Robot.* **5**(2), 164–174 (2018).

[53] M. A. Robertson and J. Paik, "New soft robots really suck: Vacuum-powered systems empower diverse capabilities," *Sci. Robot.* **2**(9), eaan6357 (2017).

Appendix A: List of symbols and abbreviations

Table A.I. *The list of symbols and abbreviations for the proposed actuator and inchworm robot.*

Symbols	Meaning	Symbols	Meaning
SRHPA	Soft-rigid hybrid pneumatic actuator	TPU	Thermoplastic polyurethane
PCTF	Proportionality coefficient between the torque and the resultant force of actuator	DoFs	Degrees of freedom
BL/s	Body length per second	MAE	Mean absolute error
r_{ab}	Vector of the line AB	n	Common perpendicular of the vectors of the lines AE and BF
h	Distance between the platform and base	θ	Angular displacement of the actuator
R_{ij}	Revolute joint	l	Length of the limb
r	Radius of the base	β	Angle between the limb and the base
F_i	Force constraint of the i-th limb	h_p	Pitch of the helical motion
F_z	External force load	M_i	Torque constraint of the i-th limb
F_a	Driving force of the bellows muscle	M_z	External torque load
l_1	Thickness of the hinges	l_2	Length of the hinges
l_3	Width of the hinges	H_0	Length of the skeleton for muscle
t_b	Thickness of the muscle	L_b	Design length of the muscle
D_1	Outer diameter of the muscle	D_2	Inner diameter of the muscle
β_1	Exterior angle of the muscle	β_2	Interior angle of the muscle